UNSTEADY THREE-DIMENSIONAL MODELING OF THE FLUID-STRUCTURE INTERACTION IN THE CHECK VALVES OF DIAPHRAGM VOLUMETRIC PUMPS

Menéndez Blanco, Alberto ; Fernández Oro, Jesus Manuel ✉ ; Meana-Fernández, Andrés

Fluid Mechanics Area, Department of Energy, University of Oviedo
C/ Wifredo Ricart, s/n. Gijón, Asturias, 33204 Spain

✉ jesusfo@uniovi.es (corresponding author)

ABSTRACT

A full 3D unsteady numerical model with dynamic meshes is developed to simulate the fluid-structure interaction in the non-returning valves of air-operated diaphragm volumetric pumps. This new three-dimensional CFD model provides a more accurate description of the flow patterns and a superior evaluation than a previous 2D model, published by the authors, regarding the dynamic response of the valves motion, which are responsible for internal volumetric losses that penalize the overall pump efficiency. Both piston-like and deformable geometries for the prescribed sinusoidal displacement of the membrane have been checked and compared in the modeling, resulting in similar behavior concerning the basic performance of the pump.

Standard operation and free-delivery conditions are exhaustively analyzed, confirming more instabilities in the check valves in case of low air-supplied pressures. In particular, the exhausting valve is found to experience severe tapping with repetitive partial closures during the forward stroke due to an intense Fluid-Structure Interaction. On the contrary, the aspirating valve presents much better sealing characteristics with a partial reopening only at the initial moments of the backward stroke.

All these numerical evidences have provided useful information for the pump manufacturers concerning the design, selection of materials and maintenance routines, which have been employed for the development of a series of new prototypes.

KEYWORDS: CFD 3D modeling; Air-operated double diaphragm pump; Dynamic mesh; Fluid-Structure Interaction (FSI); Ball valve tapping.

May, 8th, 2019.

HIGHLIGHTS

- Unsteady 3D modeling of double diaphragm pumps with a CFD dynamic mesh including FSI.
- A piston-like approach for the membrane is shown to give similar performance than a deformable diaphragm.
- Free-delivery conditions exhibit more instabilities than standard operation with ripples in the delivered flow rate.
- The exhausting valve experiences severe tapping and repetitive partial closures in the forward stroke.
- The aspirating valve presents better sealing characteristics with limited re-openings.

1. INTRODUCTION

A diaphragm pump is a volumetric fluid machine that, flexing an elastic membrane (diaphragm), pumps a (typically highly-viscous) fluid using a pair of non-return check valves introduced to prevent reverse flow. Air-operated diaphragm pumps are a common type of these pumps that consist of a double-acting set of two diaphragms and four check valves, operated with compressed air as the primary mover and alternated due to the commutation of a shuttle valve. These pumps are called as Air-Operated Double Diaphragm (AODD) Pumps.

The elastomeric diaphragm, driven by compressed air, is responsible for the reciprocating motion and the generation of a pulsating discharge flow, but it also works as a dynamic seal that removes important issues of the pump technology like internal leakages, abrasive frictions or the need for lubrication. However, the required check valves are susceptible for mechanical failures like the arising of worn balls, wedged valve seats, ball guides and/or damaged o-rings; all of them usually related to high-cycle fatigue.

The development of AODD pumps has been traditionally based on the experimental characterization of their performance [1, 2], testing materials compatibility and addressing the lifespan of the pumps when operated to different working conditions. A number of standards [2] are available in the industrial community for that purpose. Pump designers have followed trial and error procedures to present new models, most of the time inspired by the solutions of other competitors and introducing a very reduced number of well-tested and failure-proof improvements.

However, in the design stages of these new products, the introduction of new tools for a fast evaluation of the prototypes is mandatory these days. In particular, numerical methodologies emerge as a powerful method to simulate the performance of new proposals, saving costs and production times. Precisely, SAMOA Industrial S.A. [3, 4] has developed a new series of AODD Pumps, based on a revolutionary central lay-out of the internal flow passages of the pump, that has taken full advantage of modern CFD techniques for the prospective evaluation of the performance of new prototypes.

In a previous investigation of the authors, a novel methodology for the computational analysis (CFD simulation) of diaphragm volumetric pumps has been presented [5]. It

2

consists of a deformable mesh technique to simulate the unsteady full motion of the diaphragm and a fully-resolved Fluid-Structure Interaction (FSI) between the ball motion of the check valves and the pumped fluid. At the same time, other researchers have employed similar numerical techniques to study positive displacement fluid machinery. Initial contributions were focused on the global performance, trying to accurately reproduce the volumetric working principle using CFD codes. Different pump topologies were considered for the purpose, like axial piston pumps [6], air-operated piston pumps [7], plunger pumps [8] or vane pumps [9]. The aspirating characteristics of the pumps and the optimization of the basic geometrical designs have been also of interest for research [10, 11], including the influence of the fluid rheology [12]. More recently, the combination of these methodologies with cavitation models has been explored for further description of the aspirating behavior of these pumps [13, 14].

At present time, there is a major interest in the modelling of the dynamic response of check valves and its interaction with the elements responsible for the stroke motion. For that purpose, the employment of transient FSI models has been extensively introduced to describe the alternative displacement in reciprocating pumps with non-returning valves. Pioneering works were focused exclusively on the balls motion, using deforming grids [15] to simulate the opening of high-pressure safety valves [16], ball valves [17] or disk valves [18]. However, recent numerical investigations are already dealing with the combined study of the dynamic behaviour of discharge valves within complete geometries of plunger pumps [19] and reciprocating piston pumps [20] using FSI models. Complementarily, some authors have explored the application of these new techniques to describe the performance of discharge valves in linear compressors [21] and also in rotary compressors [22, 23] using ANSYS-Fluent® and ADINA® software respectively.

With respect to diaphragm pumps, there are very few available studies in the open literature nowadays. In particular, a piston-diaphragm pump with spring-loaded ball valves has been numerically simulated using immersed boundary methods and a novel FSI model [24], while the dynamic characteristics of spring-loaded port valves in a diaphragm pump has been presented lately [25]. Because of the spring stiffness employed for the pumps, these works have considered significant restrictions in the displacement of the balls, thus facilitating the numerical control and the convergence of the simulations. In case of the lack of springs, a mechanical stopper has to be modelled, as explained by the authors in its previous publication [5], with a very careful selection of the time step size in order to ensure stability and accuracy. Precisely, those preliminary results using a 2D approach have provided a reasonable agreement with respect to available experimental data and envisaged the potentiality of the spatial description of the flow to gain insight into the dynamics of the balls.

In the present contribution, the numerical methodology is extended to consider a full 3D model of the diaphragm volumetric pump. Implicit schemes are employed again for both the grid motion and the governing equations of the flow, using a URANS approach with a k-epsilon RNG turbulence model. Firstly, an equivalent cylindrical piston with the same delivery per stroke than the real membrane is employed for the volumetric displacement of the pump. Highly-refined meshes are also introduced in the vicinity of the valve seats to model correctly the FSI between the discharged flow and the non-return valves for different positions of the operating cycle. Previous 2D and new 3D results are compared for both high and low pressure regimes, analyzing in detail the

overall behavior of the pump and also the local response of the valves, responsible for oscillations and ball tapping.

Finally, an update of the model introducing the real 3D deforming geometry of the diaphragm for major fidelity is also advanced, showing a similar response with respect to the case with the simplified equivalent piston. Significant recirculations, with high rotational components of the flow in the discharge manifolds of the pump, are predicted by the 3D numerical model. Also, oscillations in the balls of the check valves with notable leakage flows and delays in the opening and closure of the valves are fully resolved via CFD simulation.

2. AIR-OPERATED DOUBLE DIAPHRAGM PUMP: BASIC DIMENSIONS AND PERFORMANCE

The AODD Pump under study is the commercial pump DP-200, selected from a new series of diaphragm pumps with a central layout, that have been developed by SAMOA Industrial SA, a European manufacturer of equipment for fluid transfer and world leader in the design of volumetric pumps [26].

Figure 1 shows a general overview with the spare parts of the pump, indicating the relevant operating components: the check valves with the balls and corresponding rings and seats; the central rod connecting both reciprocating diaphragms and the internal cavities that generate the pulsating discharge flow.

Basic dimensions and relevant geometrical data are listed in table 1. More details of the re-engineering process of the pump and its final setup for commercialization can be found in [5].
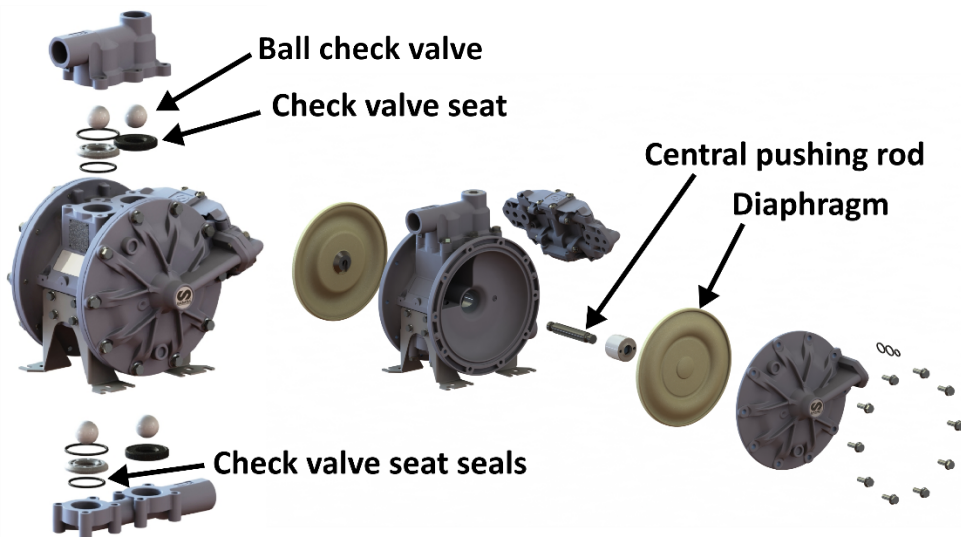
Figure 1. DP-200 pump: 3D view of the operative components.

4

Table 1. Geometrical data and operating parameters

|	
Diaphragm external diameter, D_e (mm)	200
Diaphragm internal diameter, D_i (mm)	100
Diaphragm effective diameter, D_d (mm)	150
Diaphragm stroke length, L_d (mm)	31.0
Diaphragm effective area, A_d (cm^2)	176.7
Delivery per stroke, V_d (cm^3)	548
Internal manifolds diameter, D_m (mm)	26.5
Ball diameter of check valves, D_v (mm)	31.75
Ball maximum displacement, L_v (mm)	10
Check valve effective area (max), A_v (cm^2)	4.98
Air-operation pressure, P_{air} (bar)	0-8
Pressure ratio (-)	1:1
Maximum free delivery (8 bar), Q (l/min)	200
Maximum driven velocity, n (Hz)	3.0
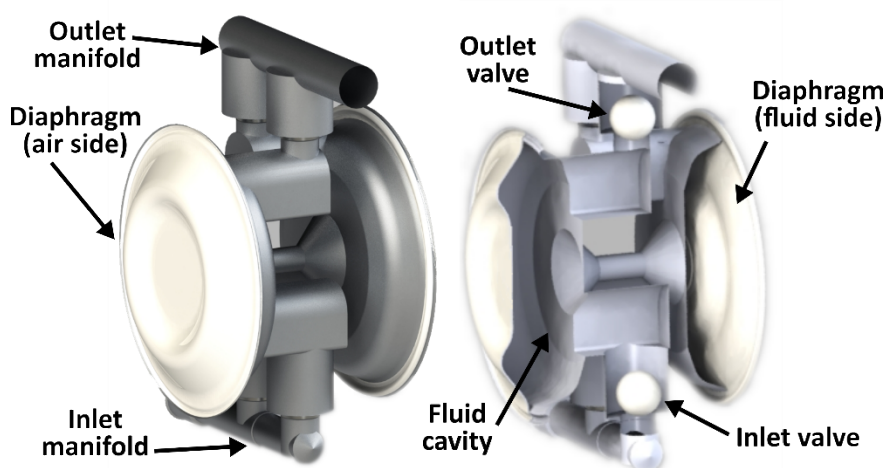
Figure 2. DP-200 pump: Rendered view of cavities and flow passages.

For the modeling purposes of this investigation, a 3D rendered view of the internal passages and cavities of the pump, see figure 2, reveals the numerical domain to be constructed. The relevant components required to simulate the working principle of the pump are identified in the left drawing, while the physical spaces to be discretized are shown in the right drawing of the figure. Taking advantage of the symmetrical geometry of the pump, only one half (one diaphragm and one set of non-return valves) of the complete body has been finally modelled.

To conclude this section, the performance curves of the pump are given in Figure 3, as provided in the technical data sheets of the pump catalogue from the manufacturer. Air-supplied pressures (2,4 & 6 bar) have been tested for different discharge pressures at a throttle valve installed in the outlet manifolds. Two pressure transducers (TE Connectivity MEAS U5244, with +/- 1% of uncertainty for a -1 to 13 bar measuring range) have been employed to obtain the pressure rise of the pump, whereas the flow rate has been measured volumetrically using an electronic balance. With this equipment, the maximum uncertainties are estimated to be 0.12 bar in the measurement of the pressure rise and a 0.7% in the retrievement of the flow rate. Black dots represent the

values obtained in the tests which have been also curve-fitted to a linear response (solid black lines referred to the left y-axis). In addition, the air consumption (grey dashed lines) has been measured using a thermal flowmeter (Testo 6442 with an operative range between 12 and 3750 lpm for a +/- 0.3% accuracy). The figure also includes efficiency isolines (grey thin lines) for the operative range of the pump. In addition, the pressure in the hydraulic chamber has been measured using a pressure transducer (ESI Genspec GS4002) with also 1% uncertainty within a -1 to 24 bar range (selected with a higher operational range to avoid damages in the sensor due to abrupt pressure peaks in the working chamber).
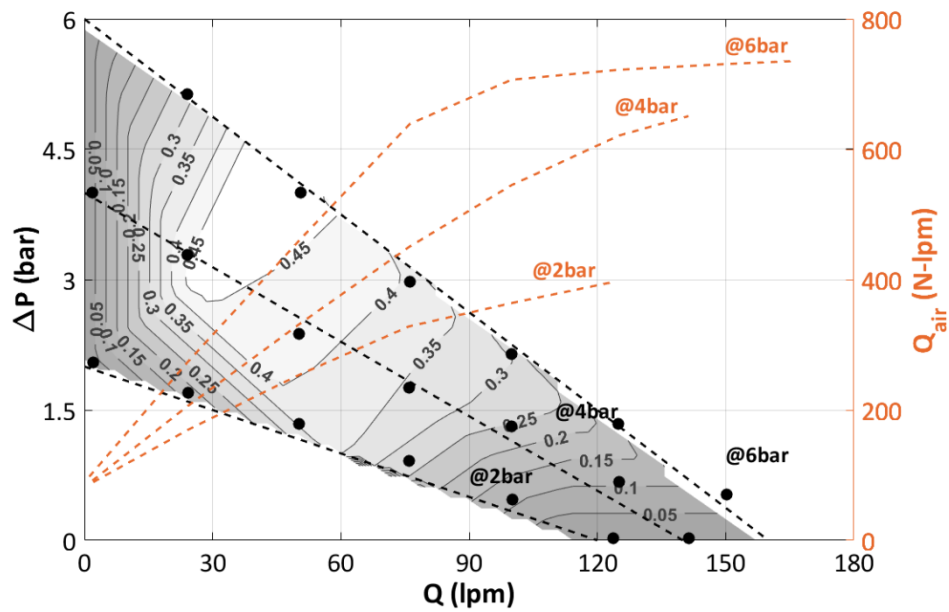

Figure 3. DP-200 pump: Performance curves for different air-supplied pressures.

3. THREE DIMENSIONAL NUMERICAL MODEL

The commercial package ANSYS-FLUENT® v16.2 [27] has been used to resolve the set of Unsteady Reynolds-Averaged Navier-Stokes (URANS) equations discretized with the Finite Volume Methodology. The three-dimensional modeling of the alternative displacement of the diaphragm, as well as the flow-induced motion of the balls in the check valves has been simulated using a dynamic mesh technique, with both remeshing and layering algorithms. Additional user-defined functions (UDFs) were also implemented for the coupled FSI resolution of the model using ad-hoc implicit algorithms [28] to speed the convergence and the numerical stability.

3.1. 3D geometry and structured mesh for a piston-like diaphragm

In order to save computational time, a first 3D approach was considered replacing the real deformable surface of the diaphragm for a piston-like and non-deformable

6

displacing surface capable to generate the same volumetric stroke than the original membrane. An equivalent diameter of the diaphragm was therefore defined and a rectangular-block strategy was implemented in the whole domain using the grid builder ANSYS-ICEM v.16.2 [29]. The complete geometry is divided and associated to different rectangular blocks to facilitate the implementation of a structured mesh in the different regions of the domain. After meshing those blocks, the grid is reshaped and projected to match the body-fitted contours of the pump. This body-fitted, modular technique allows the implementation of a structured mesh in the different regions of the domain.

The baseline mesh has been developed following the same guidelines used in the previous 2D model of the pump [30], with local refinements towards the end-walls and in the small gaps of the valve seats. Special care has been taken in the definition of the mesh associated to the balls, so y+ values between 4 and 9 could be maintained during the whole operating cycle. With respect to the piston-like diaphragm, a layering remeshing technique has taken full advantage of the linear movement of the stroke. The end-zone adjacent to the piston is enlarged or collapsed, creating or destroying complete rows of cells with a split factor of 0.4 (new cells appear when the enlargement is higher than a 140% of the original size) and a collapse factor of 0.2 (cells are removed when its length is only a 20% of the initial one). A total number of 111,575 cells has been finally adopted for the 3D modelling of the pump. Figure 4 shows the mesh density of the effective diaphragm and also the inlet and outlet manifolds connected to the working chamber. An inner view of these elements illustrates also the quality of the mesh over the valve balls on the right picture.
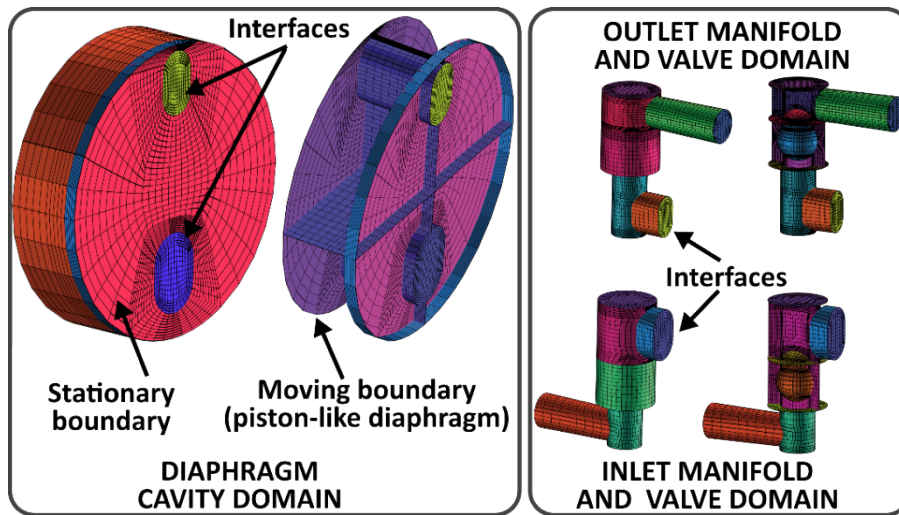
Figure 4. Mesh density in the piston-like membrane and inlet/outlet manifolds with non-return valves.

Complementarily, Figure 5 shows the end zones where the cells are created or removed (left), as well as a global view of the whole mesh (right). The figure also identifies the main boundary conditions of the model: a total inlet pressure equal to zero at the inlet of the domain and a pressure drop proportional to the kinetic energy at the outlet section. Precisely, the outlet BC is modified introducing different values of a constant K_v that represents different working conditions of the throttle valve. Besides, the

displacement of the piston-like membrane is imposed with a compiled UDF that associates a sinusoidal law to the velocity of its gravity center according to $v(t) = -\pi f L_d sin(2\pi f t)$ where L_d is the stroke length and f is the cycle frequency. Additionally, the FSI of the valves ball is also implemented using a UDF that integrates the hydrodynamic forces on the balls at the beginning of every time step to update the position of the balls. More details about the implementation of these functions is available in [5].
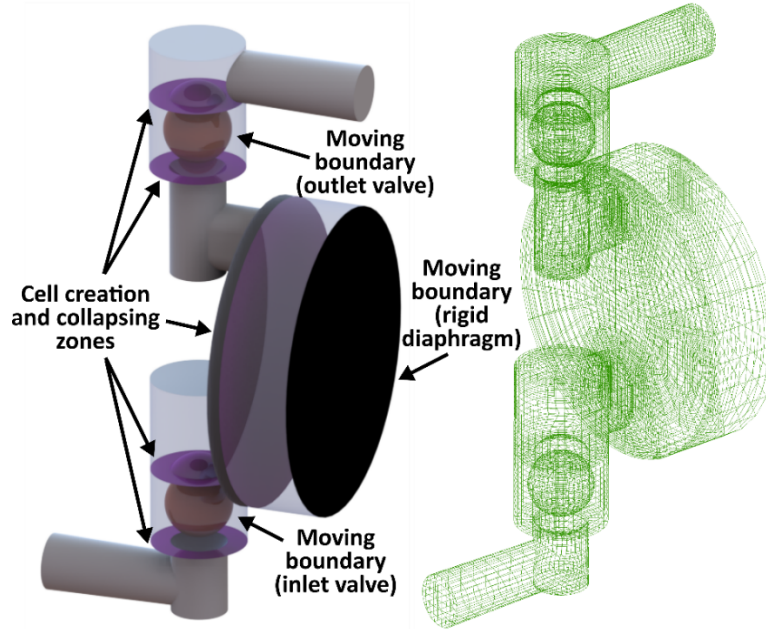
Figure 5. Mesh density in the piston-like membrane and inlet/outlet manifolds with adaptive layering mesh for the balls motion.

3.2. Numerical model and solver

The full 3D model of the pump, using deformable mesh functionalities, has been implemented in the ANSYS-FLUENT solver to resolve the unsteady RANS equations assuming incompressible, viscous flow of a single-phase Newtonian fluid (water):

- Continuity equation:

$$\frac{\partial \overline{u}_i}{\partial x_i} = 0 \tag{1}$$

- Momentum equation:

$$\rho \frac{\partial \overline{u}_i}{\partial t} + \rho \frac{\partial (\overline{u}_i \overline{u}_j)}{\partial x_j} = -\frac{\partial \overline{p}}{\partial x_i} + \mu \nabla^2 \overline{u}_i + \frac{\partial \tau_{ij}}{\partial x_j} \tag{2}$$

Where the Reynolds Stress Tensor in the momentum equation has been modelled using an Eddy Viscosity Model, according to:

$$\tau_{ij} = -\rho \overline{u_i' u_j'} = \mu_t \underbrace{\left(\frac{\partial \overline{u}_i}{\partial x_j} + \frac{\partial \overline{u}_j}{\partial x_i} \right)}_{S_{ij}} - \frac{2}{3}\rho k \delta_{ij} \tag{3}$$

being $k = \frac{1}{2}\rho \overline{u_k' u_k'}$, the turbulent kinetic energy and $\mu_t = \rho C_\mu \frac{k^2}{\varepsilon}$, the turbulent viscosity, with $C_\mu = 0.0845$. Moreover, the turbulence closure has been considered using a two-equation k-epsilon RNG turbulence model, because of its robustness and versatility. Preliminary tests with a k-epsilon Realizable model have provided very similar results (in terms of valves response and internal flow patterns), and complementary simulations with k-omega models have revealed that these low-Re models are not a recommendable option because of the excessive damping introduced when describing the instabilities of the ball valves [5]. In the case of the RNG model, these closure equations are for this case (neglecting buoyancy):

$$\rho \frac{\partial k}{\partial t} + \rho \frac{\partial (k\overline{u_i})}{\partial x_i} = \frac{\partial}{\partial x_j}\left[\alpha_k \mu_t \frac{\partial k}{\partial x_j}\right] + 2\mu_t S_{ij}S_{ij} - \rho\varepsilon \qquad (4)$$

$$\rho \frac{\partial \varepsilon}{\partial t} + \rho \frac{\partial (\varepsilon\overline{u_i})}{\partial x_i} = \frac{\partial}{\partial x_j}\left[\alpha_\varepsilon \mu_t \frac{\partial \varepsilon}{\partial x_j}\right] + C_{\varepsilon1}\frac{\varepsilon}{k}(2\mu_t S_{ij}S_{ij}) - \rho C_{\varepsilon2}\frac{\varepsilon^2}{k} \qquad (5)$$

Where the turbulent dissipation rate is defined as $\varepsilon = 2\nu\overline{s_{ij}'s_{ij}'}$, being $s_{ij}' = \frac{1}{2}\left(\frac{\partial u_i'}{\partial x_j} + \frac{\partial u_j'}{\partial x_i}\right)$; and typical coefficients $C_{\varepsilon1} = 1.42, C_{\varepsilon2} = 1.68$ and $\alpha_k = \alpha_\varepsilon \sim 1.383$ have been employed.

A second-order upwind scheme has been chosen for the spatial convective terms, with a Green-Gauss cell-based method for the computation of the spatial gradients over the diffusion terms in the momentum equation. Also, a second-order discretization has been employed for the transport equations of the turbulent kinetic energy and the turbulent dissipation rate. A segregated solver with the PISO algorithm has demonstrated an accurate compromise between stability and CPU time. A convergence criterion of 10^{-6} was fixed for the continuity equation, with a minimum threshold of 10^{-5} for the residual of the implicit update of the mesh (both must be satisfied to proceed to the next time step).

Typical time steps in the range of $5 \cdot 10^{-5}$ to $1 \cdot 10^{-4}$ have been employed as an optimal compromise between stability and economy. These values guarantee an accurate Courant number (below unity) from a physical point-of-view, so the simulation speed does not overtake the flow speed in the critical regions, especially considering the marching update of the mesh in the small gaps of the valves. Table 2 summarizes the main operational parameters for the whole numerical database simulated. Note how the time step had to be reduced for those cases with the highest frequencies and supplied pressures. Also note the extremely high number of time steps required (around ten thousand) to describe a complete operative cycle of the pump. Approximately, 450 hours (3-4 weeks) of CPU time were necessary to resolve one cycle of the 3D model with 111K cells using a 4-nodes Intel Core i7-5820K single PC at 3.3 Ghz and 64Gb RAM.

Table 2. Numerical database. Outlet BC and time step sizes.

Test No.	Supplied pressure (bar)	Discharge pressure, P_{RMS} (bar)	Loss coefficient, K_v (-)	Driving frequency (Hz)	Time step, Δt (s)	N° time steps per cycle (-)
#1	2	0	0	1.85	$1\cdot10^{-4}$	5,400
#2	2	1.16	75.1	1.0	$1\cdot10^{-4}$	10,000
#3	4	0	0	2.45	$1\cdot10^{-4}$	4,080
#4	4	1.99	62.1	1.4	$1\cdot10^{-4}$	7,140
#5	4	3.65	1411	0.45	$1\cdot10^{-4}$	22,220
#6	6	0	0	2.7	$5\cdot10^{-5}$	7,400
#7	6	1.97	32.5	1.8	$5\cdot10^{-5}$	11,110
#8	6	3.63	139.9	1.25	$1\cdot10^{-4}$	8,000
#9	6	4.14	500.8	0.75	$1\cdot10^{-4}$	13,330

3.3. 3D model with deformable diaphragm

An additional modeling effort has been considered implementing the real deformation of the diaphragm in the 3D model. For that purpose, the piston-like membrane has been replaced by a flexible diaphragm composed of a rigid, internal circular plate, and a surrounding, deformable annular region (see Figure 6). The circular plate is displaced in a rigid-body fashion, following the same sinusoidal law that was previously prescribed for the piston-like membrane. In the case of the mesh elements placed over the circumferential annular region, the amplitude of the stroke has to be calculated as a function of the local radius in order to preserve the integrity of the diaphragm.

Because of this new topology, the working chamber had to be discretized using a tetrahedral mesh, which had to be also updated using the remeshing technique. This dynamic technique introduces by default a spring-based smoothing method that allows a simple redistribution of the mesh when the boundary displacements are small. In case of large displacements compared to the local cell sizes, the cell quality can be deteriorated leading to the degeneration of the mesh. To circumvent this problem, those cells violating the skewness or size criteria are agglomerated and further remeshed to satisfy the skewness criterion while the solution is interpolated from the old cells. In this case, a spring factor of 0.9 has been fixed for minimum and maximum cell sizes of 2 and 10 mm respectively, with a maximum cell skewness of 0.7. The updating interval for the mesh resizing was completed every 10 time steps. The baseline mesh for this new 3D model presented a hybrid grid with a total number of 101,957 elements. Despite this new 3D model has been meshed with a 10% lower cells than the piston-like approach, the CPU time has been notably increased, reaching up to 550 hours to complete one working cycle with the same workstation. Hence, introducing a 1.1 correction factor to discount the unequal number of cells, the remeshing technique resulted approximately 30% slower than the layering technique. Due to this extra computational costs, the use of a deformable approach should be justified only in case of remarkable differences in the results between both models.

To compare the results of this model with respect those given by the piston-like membrane, the cases for the free delivery output (tests #1, #3 and #6 from Table 5) were

repeated using this new deformable diaphragm. The findings and similitudes are shown later in section 4.5 of the paper.
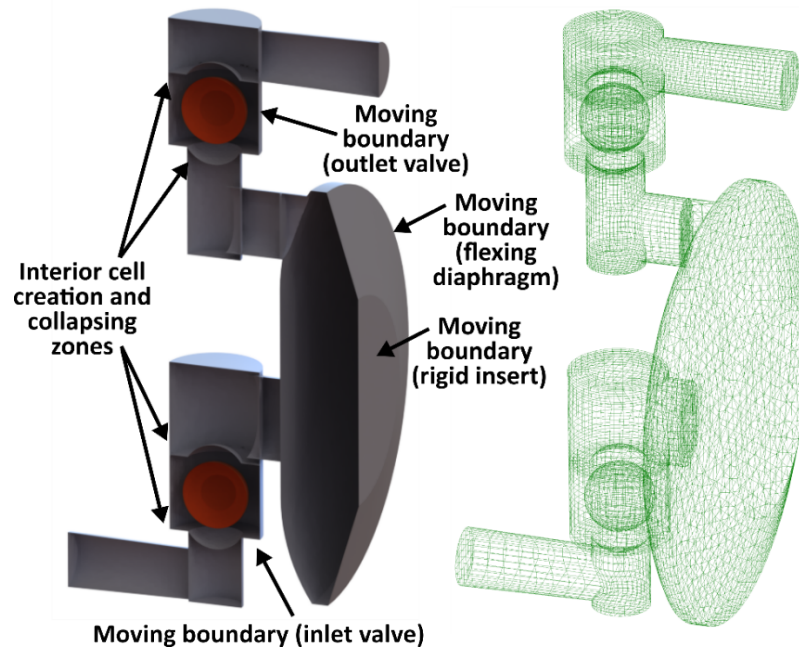

Figure 6. Mesh density in the deformable diaphragm and inlet/outlet manifolds with adaptive layering mesh.

4. RESULTS AND DISCUSSION

4.1. Comparison of performance curves

Firstly, the delivered flow rate as a function of the discharge pressure, calculated by the 3D numerical model, is compared with the experimental curves in Figure 7. The computed flow rates are duplicated for the comparison due to the symmetrical boundary conditions imposed. It is noticeable how the numerical model reproduces the linear decay observed experimentally for the delivered flow rate as the discharge pressure is increased. For low-to-moderate operating pressures (2 and 4 bar), there is also a good correspondence in the estimated values, with maximum errors up to a 6% (see table 3 below). For high-pressure condition (6 bar), although the overall trend is reasonably captured, the results present more deviations, with maximum differences in the order of a 19% for the flow rate estimation. This can be attributed to the influence of the high air-supplied pressure on the stability of the stroke frequency, as discussed in the following section.

Table 3. Discrepancies between numerical and experimental results.

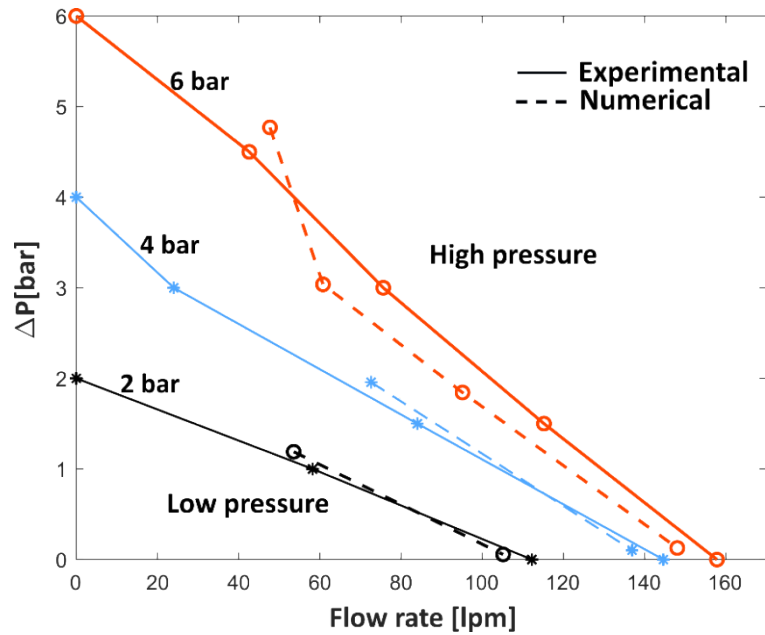|	Air-supplied Pressure		
Outlet Discharge pressure	@2 bar	@ 4 bar	@ 6 bar
Low Pressure (free-delivery)	6.3 %	5.3 %	6.2 %
High Pressure (standard operation)	8.1 %	13.4 %	19.0 %

Figure 7. Comparison of experimental and numerical performance curves.

4.2. Pressure evolution in the working chamber

The unsteady evolution of the pressure in the working chamber of the diaphragm is plotted for two representative situations in Figure 8, comparing both numerical and experimental data. Previous results obtained with a 2D model are also included in the comparison. In particular, the left plot provides the results in case of high air-supplied pressures (@6 bar) for a low discharge pressure (1.5 bar at the outlet), whereas the right plot shows also low exhausting pressure (1 bar) but now in case of low supplied pressure (@2 bar). Note that the experimental curve has been obtained after ensemble-averaging the instantaneous, original signal (measured for more than 20 operating cycles), in order to remove noise-to-signal perturbations.
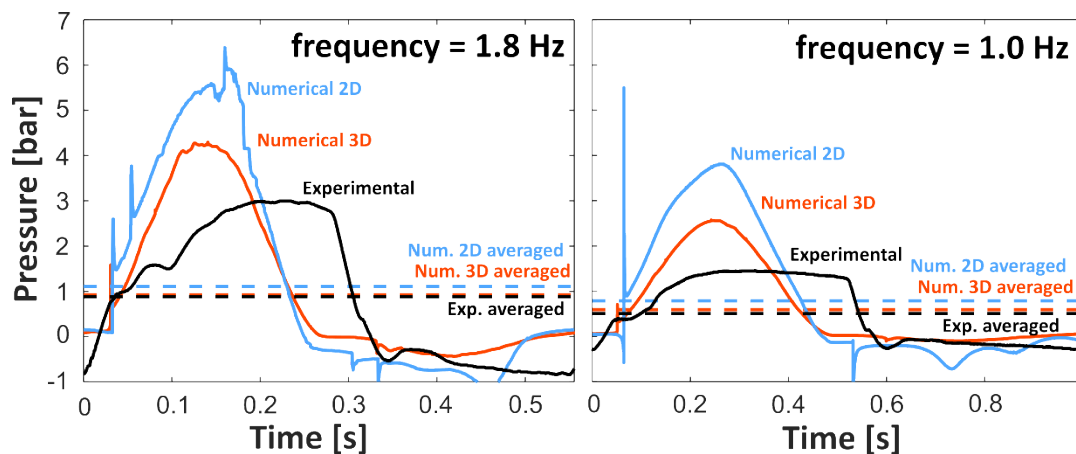

Figure 8. Comparison of experimental and numerical evolutions of the pressure in the working cavity: High (left plot) and low (right plot) air-supplied pressures for standard operation.

12

It is evident that 3D results are resembling with higher fidelity the pressure evolution in the diaphragm cavity. At more demanding conditions (left plot), the real pressure is much more sinusoidal, revealing a significant two-way influence of the air-supplied pressure on the dynamics of the membrane. This explains the higher discrepancy observed in the results of the performance curves. The numerical evolutions are also following a sine wave (imposed by the prescribed motion of the piston), although 2D results exhibit more instabilities with poorer performance. However, it is really significant that the RMS value (mean values in dashed lines) of the pressure fluctuations in the cavity is coincident for the experimental and the 3D results (the value is overpredicted by the 2D model).

In the case of low air-supplied pressure (right plot), the experimental pressure in the diaphragm chamber follows a stepped evolution, rather than a sinusoidal behavior. Precisely, this suggests a less influence of the hydraulic condition over the instantaneous pressure of the supplied air; thus, providing more validation to the assumption of a prescribed sine wave in the membrane (reproduced again in both 2D and 3D results). Note again the perfect match between the time-averaged value (RMS mean values in dashed lines) of the pressure in the experimental and 3D numerical results. On the contrary, 2D results exhibit a clear overprediction in the averaged value and also pressure peaks during the opening and closure of the non-return valves.

Following, detailed results concerning flow structures and response of the dynamic elements inside the pump will be discussed below, for the situations of high (6 bar) and low (2 bar) air-supplied pressures (equivalent to high -1.8 Hz- and low -1.0 Hz- driving frequencies). Also 1.5 to 1.0 bar outlet pressures (standard operation) and free-delivery conditions will be analyzed.

4.3. Standard operation. Comparison of 2D and 3D results.

Typically, these AODD pumps perform for an operative outlet pressure in the range of 1.0 to 1.5 bar, despite of the significant penalty in efficiency. This is a quite common situation for industrial applications of diaphragm volumetric machines which is usually denoted as "standard operation" by the manufacturer.

The description of the internal behavior of the pump is now presented for high delivered flow rates (i.e., high air-supplied pressures @6 bar) and also for low volumetric flow rates (i.e., low air-supplied pressures @2 bar).

4.3.1. Delivered flow rate and response of non-return valves

Figure 9 compares the evolution of the flow rates, the pressure in the cavities and the unsteady response of the non-return valves over a typical operating cycle of the pump between 2D and 3D models for a high driving frequency. Two-dimensional results (left subplots) present abrupt pressure peaks in the cavity (attenuated later in the outlet

pressure) with a characteristic (unrealistic) bump between 3T/8 and T/2, corresponding to a partial closure of the discharge upper valve. The aspirating valve (blue line in the third subplot) also exhibits instabilities when the pump is suctioning fluid, thus leading to a less pronounced closure that has no effect on the evolution of the incoming flow rate.

Alternatively, 3D results (right subplots) provide more coherent evolutions, with real flow rates in the discharging valve a bit lower than the expected theoretical values (see comparison between solid and dashed lines in the central subplot). Also, the response of the non-return valves is clearly more dynamic, with a first rapid closure followed by a series of two swift rebounds (tappings). A similar behavior is observed in the aspirating valve during the second half of the cycle between the top and bottom dead centers of the stroke.
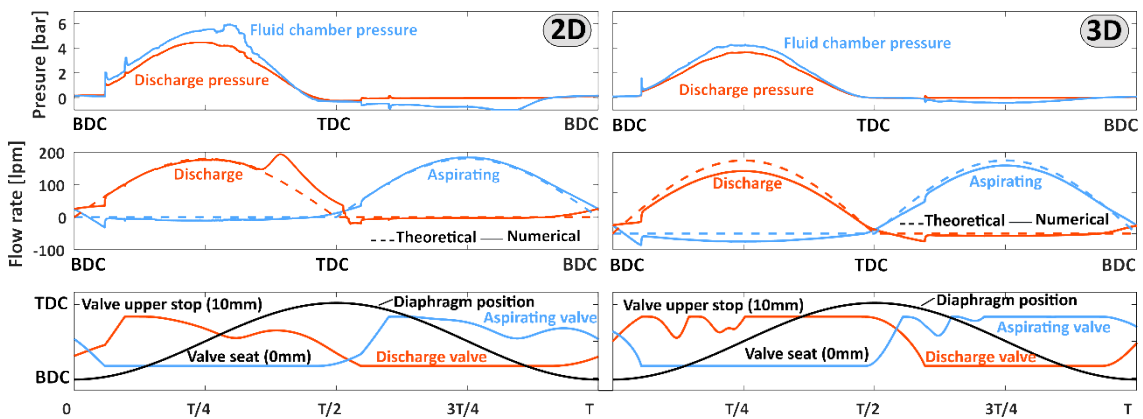
Figure 9. Comparison of temporal evolutions of the pressure, flow rate and check valves response during the diaphragm cycle between 2D (left) and 3D (right) results, in the case of high air-supplied pressure.

Figure 10 provides the same analysis but in the case of low air-supplied pressure (i.e.; low driving frequency and thus low delivered flow rate). In this case, overall 2D and 3D results are much more coincident, although the unrealistic overflow (bump) in the discharging valve is still present. Because of the lower frequency, the instabilities in the balls of the valves are more evident. This is particularly pronounced in the 3D model, where the ball is continuously oscillating (up to four times) during the first half of the cycle.
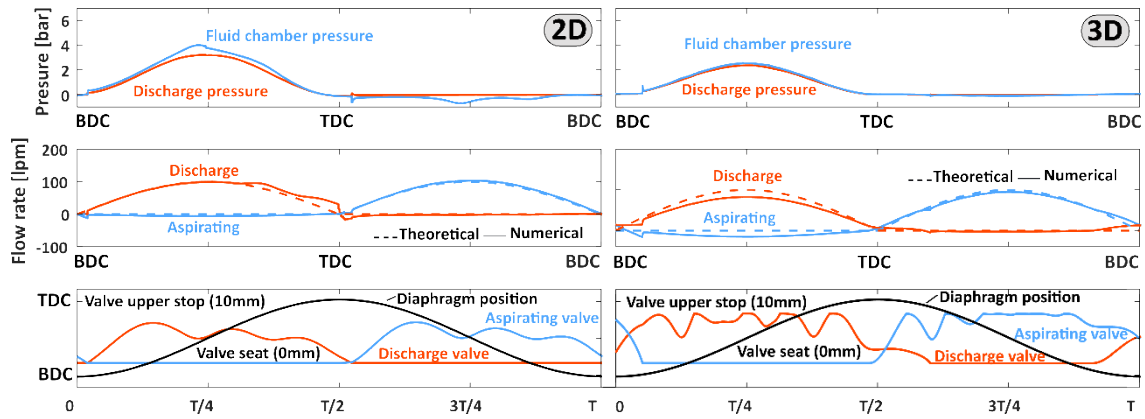
14

Figure 10. Comparison of temporal evolutions of the pressure, flow rate and check valves response during the diaphragm cycle between 2D (left) and 3D (right) results, in the case of low air-supplied pressure.

4.3.2. Evolution of the opening in the non-return valves: comparison of 2D and 3D simulations

A closer look to the oscillating behavior of the check valves in the case of a high driving frequency for the standard operation cases is performed in the following figures 11 (for the discharging valve) and 12 (for the aspirating valve). In particular, the partial closures of the valves are illustrated with the instantaneous flow fields (contours of velocity magnitude) around the balls for further physical insight. The graphics have been completed introducing the evolution of the instantaneous force over the balls to understand the going ups and downs observed.

In the case of the exhausting valve (figure 11), 2D results predict a single oscillation, close to the end of the discharge hemicycle, associated to an abrupt rise of the force over the ball. After the initial stroke of the membrane (first peak in the force evolution) has provoked the complete displacement of the ball (first picture), the ball begins to fall downwards. At that moment, two high velocity jets (second picture) are established around the ball, thus reducing the local pressure and generating a significant suction that tends to re-open the gap (third picture). Finally, with the end of the forward stroke, the ball returns to the seat (forth picture). Note the unrealistic formation of those high velocity jets around the 2D circle as a consequence of the block imposed by the geometrical restrictions of a two-dimensional domain.

Alternatively, 3D results (shown through a transversal view in the figure) reveal a practically instantaneous opening of the valve (first picture), followed by a very fast, partial closure (second picture) which is rapidly arranged due to the arising of a high velocity region (third picture) when the forward stroke is approaching to its maximum acceleration (at T/4). After that, a second rebound is finally rectified due to the reinforcement of the incoming fluid driven by the membrane (see the high velocity region in the vicinity of the ball). The high velocity jet induces an intense suction that maintains the valve opened and a high force (forth picture) during the second half of the hemicycle.

15

886
887
888
889
890
891
892
893
894
895
896
897
898
899
900
901
902
903
904
905
906
907
908
909
910
911
912
913
914
915
916
917
918
919
920
921
922
923
924
925
926
927
928
929
930
931
932
933
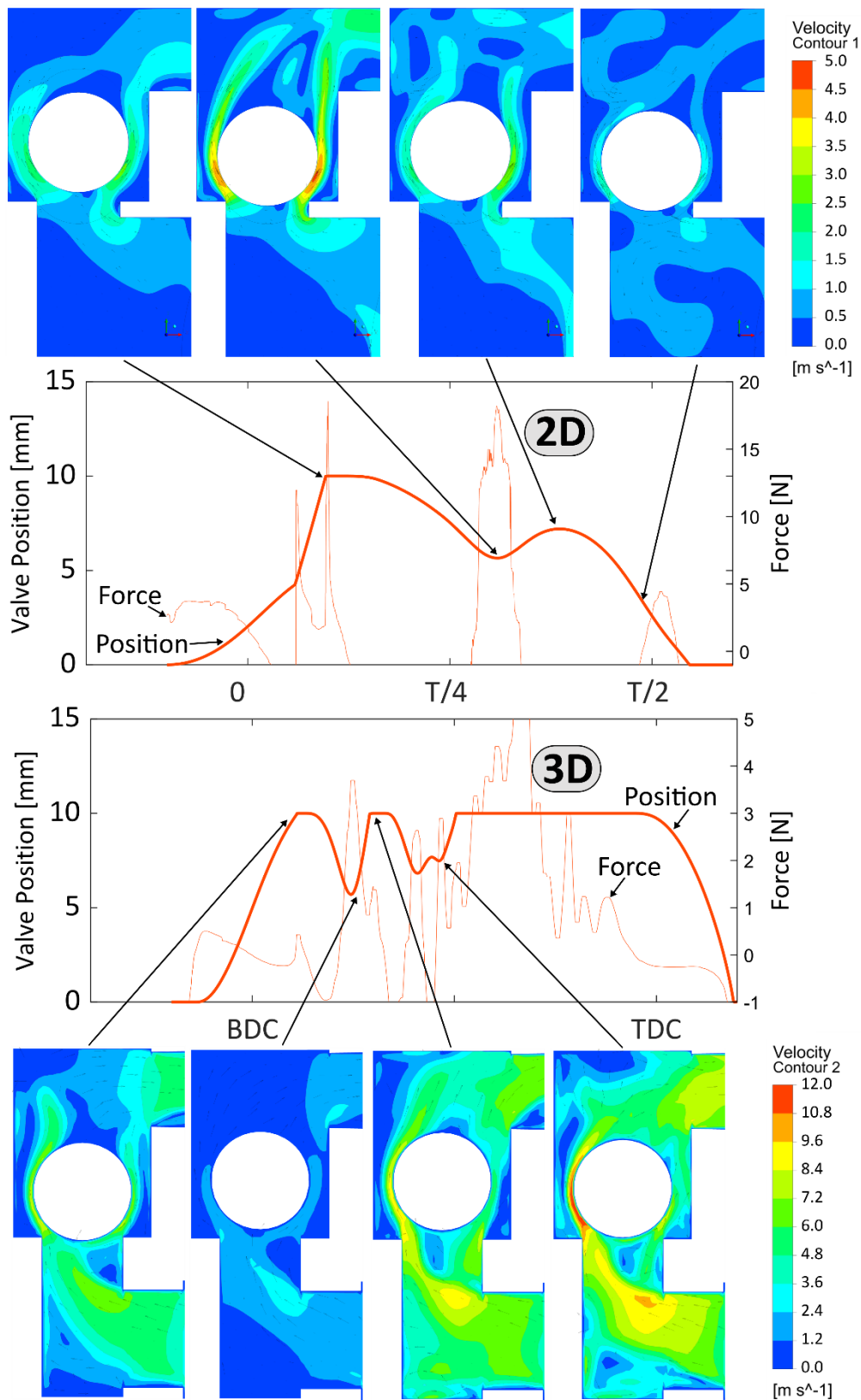934
935
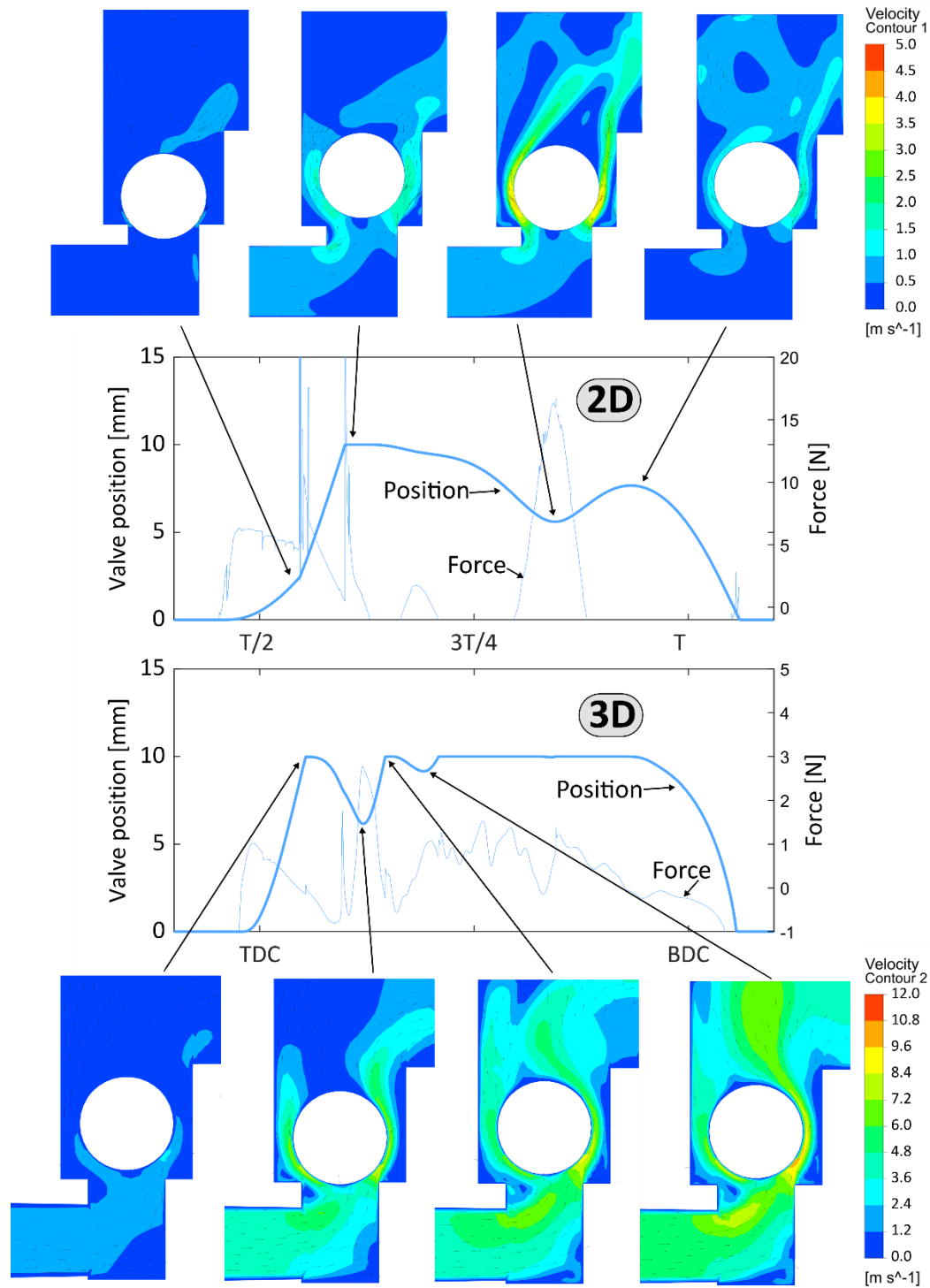936
937
938
939
940
941
942
943
944

Figure 11. Response of the discharging non-return valve over the operative cycle for high air-supplied pressure. Comparison of 2D (top) and 3D (bottom) computations.

945
946
947
948
949
950
951
952
953
954
955
956
957
958
959
960
961
962
963
964
965
966
967
968
969
970
971
972
973
974
975
976
977
978
979
980
981
982
983
984
985
986
987
988
989
990
991
992
993
994
995
996
997
998
999
1000
1001
1002
1003

Figure 12 provides similar conclusions with respect the aspirating valve. In this case, the ball dynamics and the surrounding flow patterns are induced by the underpressure associated to the backward stroke. Consequently, the flow patterns are more uniform and high velocity jets are less pronounced with more evenly distributions around the check valve.

Figure 12. Response of the aspirating non-return valve over the operative cycle for low air-supplied pressure. Comparison of 2D (top) and 3D (bottom) computations.

4.3.3. Evolution of the flow patterns within the pump internal cavities: comparison of 2D and 3D maps

The comparison of 2D and 3D models is finished addressing the differences in the internal flow patterns within the pump in the case of a high air-supplied pressure (@6 bar) for standard operation (figures 13 and 14 respectively).

Firstly, figure 13 shows the description of the 2D flow patterns (contours of velocity magnitude) at four intermediate positions of the operating cycle. Only at t=T/4 the exhausting valve is partially opened; in the rest of the snapshots, it is practically closed. It is quite significant the appearance of several recirculating cells of fluid in the internal passages; especially in the final contour at the BDC of the diaphragm (t=T), with up to 5 recirculating cells. Note also the flow separation in the outlet manifold at t=T/4 and the accurate guidance of the suctioning flow when it is introduced in the working chamber of the membrane (t=3T/4).
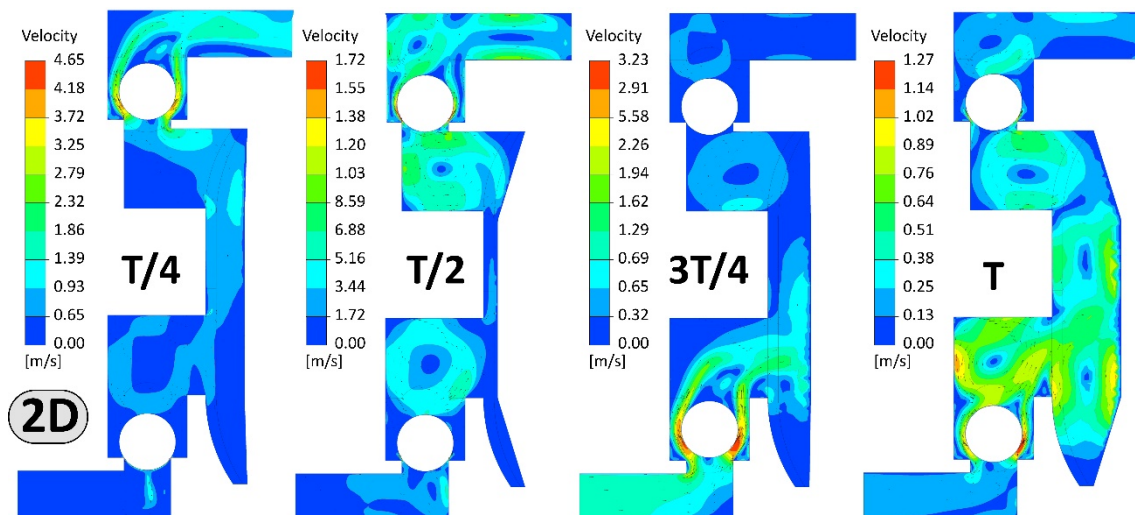

Figure 13. 2D description of flow patterns for high air-supplied pressure.

On the contrary, results in figure 14 does not present any significant flow recirculation in the domain during the whole cycle for 3D computations. Rotational components of the flow velocity at the outlet seem to have been also mitigated. In addition, the high-velocity jets developed around the balls in the check valves are clearly displaced towards the left in the case of the discharging valve and the right in the aspirating valve. This is clearly an effect induced by the piston-like diaphragm when suctioning or driving the flow. Note also that 3D results exhibit lower stagnation conditions than 2D maps.
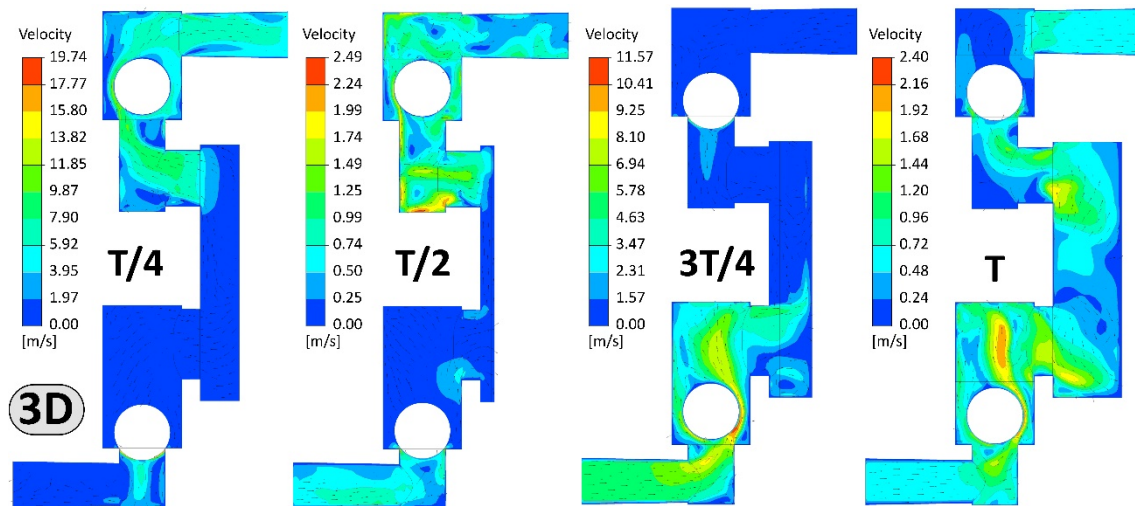
18

Figure 14. 3D description of flow patterns for high air-supplied pressure.

4.4. Free-delivery conditions.

When maximum output flow rates are required, it is usual to operate the diaphragm pump under free-delivery conditions. This is a typical situation found when a tank is been draining. Under this scenario, the pump is more susceptible to internal instabilities and oscillations leading to ball tappings and more vibration due to the highest frequencies supported (up to 2.8 Hz). The numerical data presented in this section concerns to 3D results only.

4.4.1. Evolution of discharged flow rate and pressure as a function of the response of the non-return valves.

Figure 15 presents the evolution of the pressure in the working chamber and the delivered flow rate in the case of a high air-supplied pressure (left plots). The pressure in the cavity of the diaphragm is associated to the pressure loss in the internal circuit of the pump, since the discharged pressure is atmospheric. Note that pressure peaks are more pronounced than in the case of standard operation. Furthermore, when the working chamber is aspirating (see blue line in the top left plot), significant under pressures are attained in the pump (close to -1 bar) that makes it susceptible for cavitation inception. Another important feature is that volumetric losses are increased with respect to the standard working operation.

Right plots in figure 15 reveal the evolution of the balls motion (position in solid, thick lines and velocities in solid, thin lines) in the valves with their corresponding hydrodynamic forces exerted by the fluid (dashed lines). Oscillations in the balls are associated to maximum velocities in the range of 1 m/s, with a maximum force of 100 N. These values are observed during the closure of the aspirating valve. It is also clearly demonstrated that a delay around one eight of the whole cycle period is established in the balls for a complete closure (thus, far away from being instantaneous).
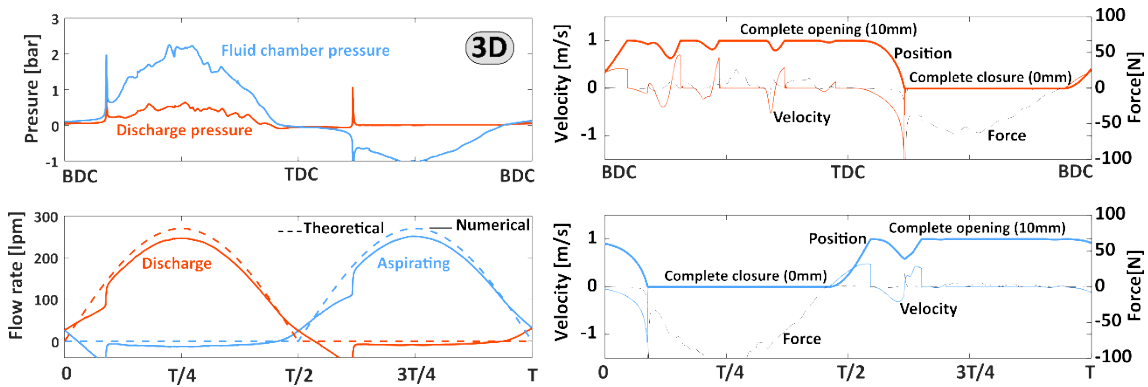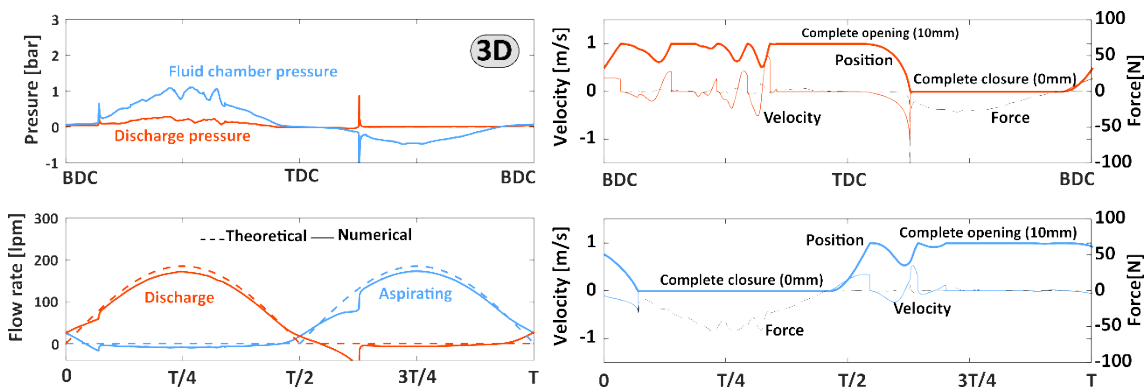
19

Figure 15. Temporal evolution of pressure and flow rate (left) and response of the non-return valves (right) in the case of free delivery for high air-supplied pressure.

Additionally, figure 16 presents similar results but now in the case of a low air-supplied pressure. The pressure in the working chambers is significantly lower, so the volumetric efficiency is clearly improved. The underpressure during the aspiration stroke is also relaxed. Concerning the instabilities in the balls, the evolution in the exhausting and aspirating values differ notably. The exerted forces are also reduced (below 50 N) due to the less demanding conditions.

Figure 16. Temporal evolution of pressure and flow rate (left) and response of the non-return valves (right) in the case of free delivery for low air-supplied pressure.

4.4.2. Evolution of flow contours in the cavities under free-delivery conditions.

Figure 17 illustrates the evolution of the velocity maps in the working chamber (3D results only), which can be compared to previous results shown in Figure 14 in the case of standard operation.

Overall patterns are similar, but higher gradients are identified in the case of free-delivery condition. In particular, the velocity gradients nearby to the discharge valve at t=T/4 are significantly higher. Also, at t=3T/4, the valve side close to the diaphragm exhibits higher velocities as a consequence of the higher driving frequency of the piston.
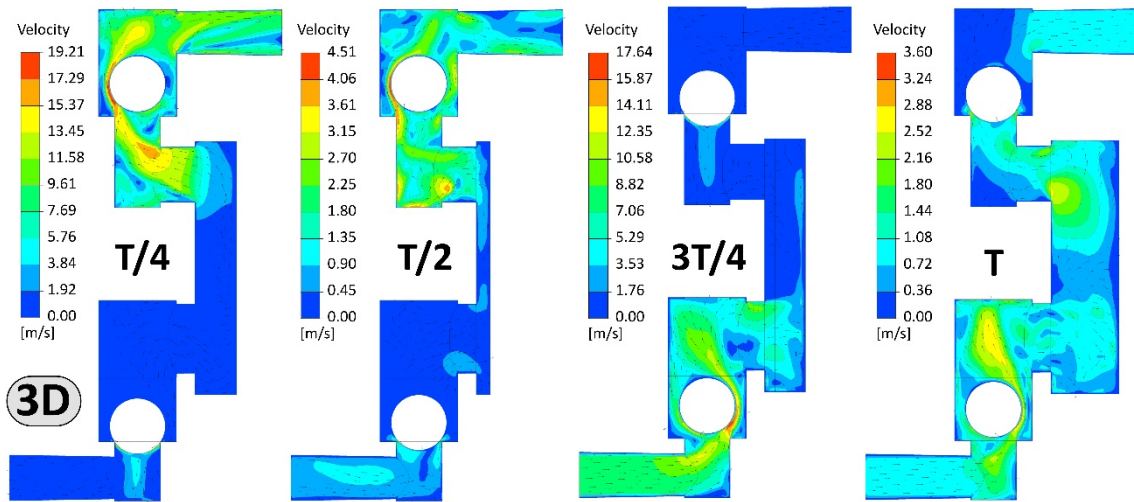
20

Figure 17. 3D description of flow patterns under free-delivery conditions.

To conclude, an additional figure showing the main streamlines (released from the reciprocating membrane) within the pump cavities for both forward and backward strokes is introduced in figure 18. This representation provides a comprehensive 3D view of the complexity of the flow in the non-return valve. In the left, a recirculation zone is clearly identified upstream of the discharge valve, also complemented with a high rotational area of flow in the discharge manifold. On the other hand, the right picture demonstrates that there is a lower vorticity downstream of the aspirating valve (more space is available to allow a more uniform flow associated to the suction induced by the piston) and even less recirculation upstream of the valve. Both images also reveal internal flow leakages in the ball seats due to the partial re-opening of the valves.
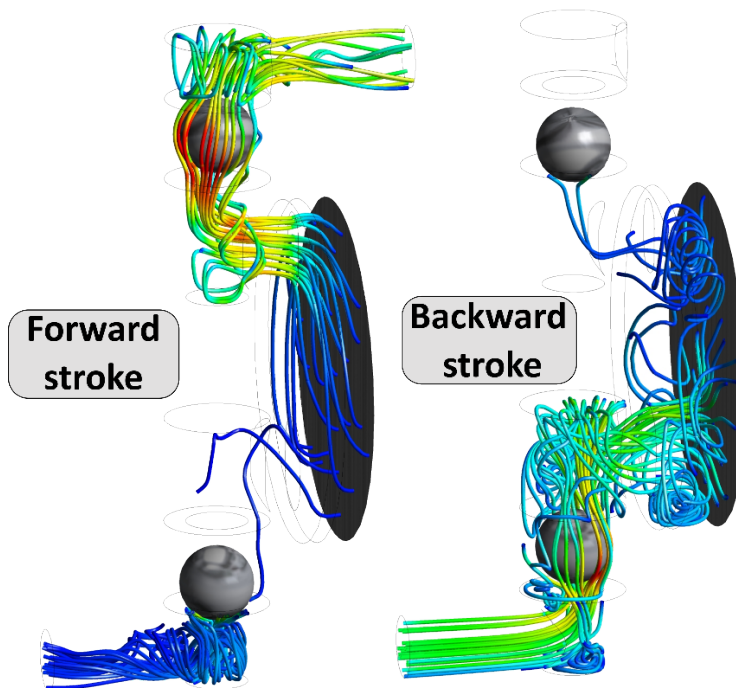

Figure 18. Streamlines in the internal cavities of the pump. Comparison of forward (left) and backward (right) strokes at free-delivery conditions.

21

4.5. Deformable (real) diaphragm VS piston-like (approach) diaphragm.

The paper is concluded comparing overall results of the 3D numerical model developed with the deformable diaphragm with respect to previous results of the piston-like diaphragm approach shown earlier. The objective is to show if the extra computational costs associated to the remeshing technique are worthwhile or if it is sufficient to use a 3D cylinder approach to obtain sufficiently reliable results.

Figure 19 (right column) reveals that overall behavior of the main fluid-dynamic variables is quite similar between both models. However, the pressure in the cavity of the diaphragm is less sinusoidal as a consequence of the early deceleration of the inner, rigid circular plate. Hence, a plateau is established in the pressure distribution because of the reduced extension associated to the final stages of the diaphragm stroke. This effect has an impact on the evolution of the discharge non-return valves modifying the response of the balls with two re-openings only. Alternatively, the evolution of the aspirating valve is practically identical between both models, although the volumetric efficiency is significantly improved in the case of the deformable diaphragm.
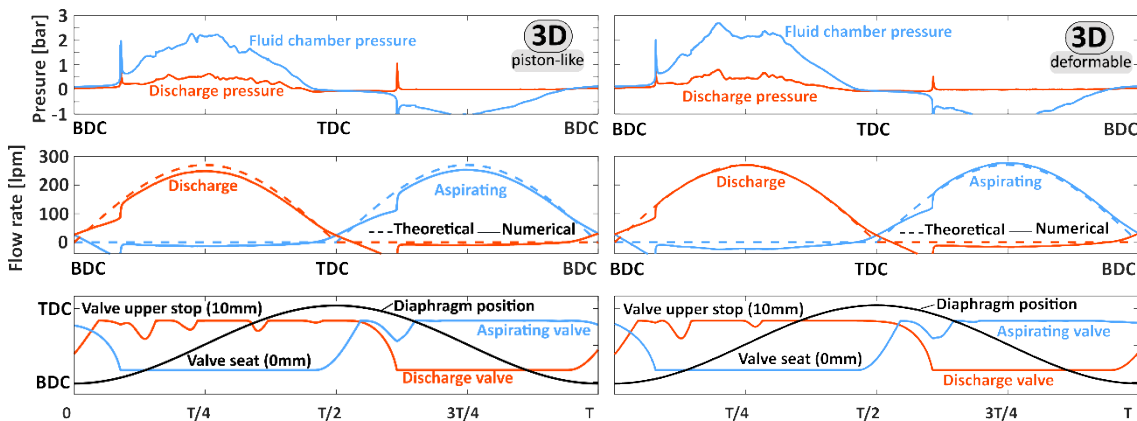

Figure 19. Comparison of temporal evolutions of the pressure, flow rate and check valves response during the diaphragm cycle between 3D, piston-like model (left) and 3D deformable diaphragm (right) results.

Finally, figure 20 illustrates the differences in the flow patterns, in terms of velocity fields, between the deformable and the piston-like approaches. In the left, velocity maps are represented at T/4 during the maximum impulse of the forward stroke to illustrate how the flow driven by the diaphragm passes through the discharging valve. In the case of the deformable diaphragm, the flow is better introduced in the outlet port, with a more progressive and well-guided high-velocity jet passing around the ball. On the contrary, in the piston-like model, there is a significant portion of the flow recirculating in the rectangular cavity that connects the working chamber with the outlet manifold, thus justifying the higher volumetric losses observed in previous figure 19.

In the right-hand side, the comparison of the velocity maps at 3T/4 during the backward stroke reveals marginal differences between the models. It is only significant that the deformable model has more space available in the lower part of the diaphragm, so the pressure gradient that it is suctioning is more progressively distributed in the chamber. This leads to better aspirating conditions which are perceived as a lower flow leakage for the inlet check valve.
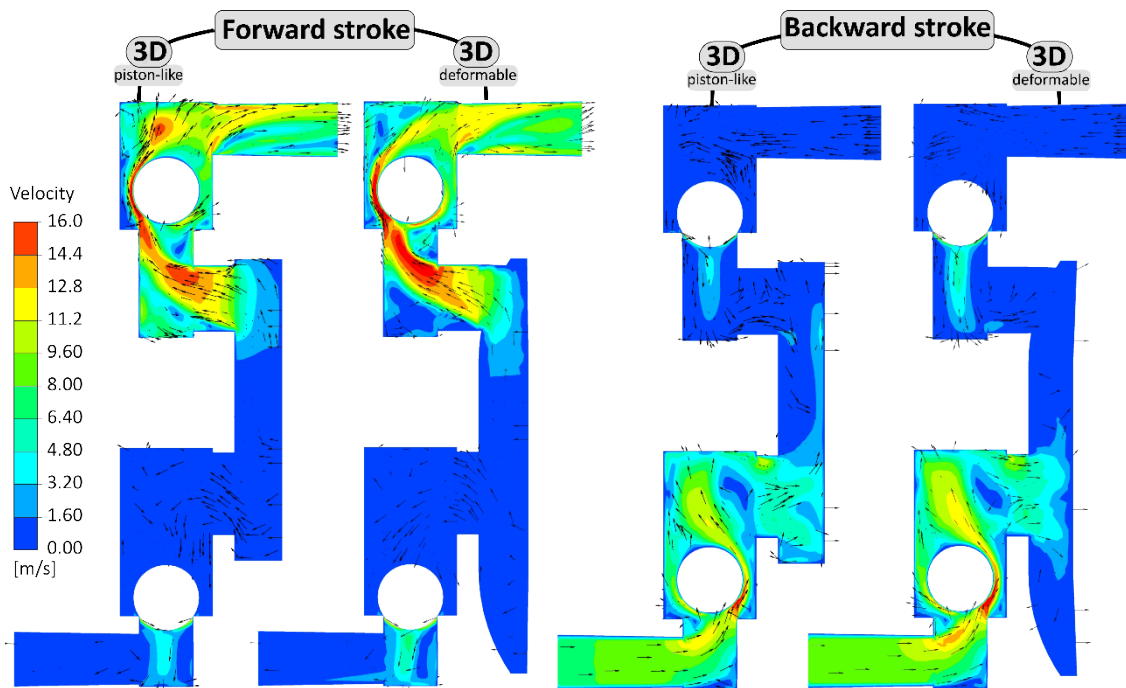

Figure 20. Comparison of flow patterns in the cavities between 3D piston-like model and 3D deformable diaphragm model.

5. CONCLUSIONS

A full 3D, unsteady model with dynamic meshes for the CFD simulation of Air-Operated Double Diaphragm (AODD) Pumps has been developed and tested for different operating conditions. This new model has taken full advantage of a previous two-dimensional numerical methodology presented recently by the authors for the simulation of this type of positive displacement pumps.

Precisely, new 3D results have been compared to previous 2D data, in terms of overall performance, volumetric efficiency of delivered flow rate and response of non-return valves to confirm the convenience of using fully 3D models to describe these volumetric pumps.

In order to save computational times, a piston-like membrane was firstly employed, providing an equivalent volumetric displacement to the real deformable diaphragm that allowed the consideration of more economic layering algorithms. Finally, a flexible,

deformable diaphragm was also modelled for completeness, concluding that overall behavior and basic performance of the different elements are reasonably reproduced with the piston-like model.

Experimental validation showed that the evolution of the performance curves was satisfactorily captured with the 3D models, also indicating that the selection of the mesh size and its quality and the time step adopted were correct. Local pressure measurements in the diaphragm cavity and its comparison with the numerical data revealed differences in the evolution over the operative cycle, but with identical time-averaged effects.

In the case of standard operation, low air-supplied pressures (@2 bar) result in higher instabilities with more ball tapping, especially in the outlet non-return valve (up to four partial re-openings). When the supplied pressure is increased (@6 bar) this phenomenon is mitigated, presenting lower oscillations (only two re-openings are found in the initial stages of the forward stroke) and better volumetric efficiencies.

It is also found that the 2D model introduces excessive dumping, under-predicting the strong dynamic response of the fluid-structure interaction established between the balls and the flow patterns. With the 2D models, a slow response with minor oscillations that are severely attenuated is resolved only. On the contrary, 3D models provide a more realistic and precise description of the rapid, inertial effects in the valves.

In the case of free-delivery conditions, overall results are found to be very similar to those obtained for the standard operation. However, the pressure in the diaphragm cavity during the backward stroke (aspirating conditions) drops significantly in this case, reaching extremely large under-pressures that could make the pump susceptible for cavitation inception. In addition, the volumetric losses are also increased with respect those observed in the standard operation, as expected from the efficiency map pf the pump.

Finally, it is quite relevant that, for all the cases analyzed, the instabilities in the exhausting valve are clearly more important than in the aspirating valve. It is concluded that the inlet valve presents much better sealing characteristics than the discharge valve, with a typical partial re-opening only at the very beginning of the backward stroke. This finding is useful to provide basic guidelines concerning the design, selection of materials and maintenance routines of the different constructive elements of the pump.

REFERENCES

[1] ANSI/HI. 10.1-10.5, "Air Operated Pumps for Nomenclature, Definitions, Application and Operation," *Hydraulic Institute*, 2010.

[2] ANSI/HI. 10.6, "Air Operated Pump Tests," *Hydraulic Institute*, 2004.

[3] Bahrton, S., "Reversing Valve for a Diaphragm Pump," *US Patent* 6419463 B1, 2002.

[4] González-Moratiel, A., "Double-Membrane Central-Flow Pump," *EP Patent* 2573397 A1, 2013.

[5] Menéndez-Blanco, A.; Fernández Oro, J.M.; Meana-Fernández, A., "Numerical Methodology for the CFD Simulation of Diaphragm Volumetric Pumps," *International Journal of Mechanical Sciences*, vol. 150, pp. 322–336, 2019.

[6] Kumar, S.; Bergada, J.M.; Watton, J., "Axial Piston Pump Grooved Slipper Analysis by CFD simulation of Three-Dimensional NVS Equation in Cylindrical Coordinates," *Computers & Fluids*, vol. 38, pp. 648–663, 2009.

[7] Menéndez-Blanco, A.; Fernández Oro, J.M., "Unsteady Numerical Simulation of an Air-Operated Piston Pump for Lubricating Greases using Dynamic Meshes," *Computers & Fluids*, vol. 57, pp. 138–150, 2012.

[8] Ragoth, R.S.; Nataraj, M., "Study on Performance of Plunger Pump at Various Crank Angle Using CFD," *Engineering Science and Technology: An International Journal*, vol. 2 (4), pp. 549–553, 2012.

[9] Frosina, E.; Senatore, A.; Buono, D.; Stelson, K.A.; Wang, F.; Mohanty, B.; Gust, M.J., "Vane Pump Power Split Transmission: Three Dimensional Computational Fluid Dynamic Modeling", *Proceedings of the ASME/BATH 2015 Symposium on Fluid Power and Motion Control*, Chicago, IL (USA), October 12–14, 2015.

[10] Iannetti, A.; Stickland, M.T.; Dempster, W.M., "A Computational Fluid Dynamics Model to Evaluate the Inlet Stroke Performance of a Positive Displacement Reciprocating Plunger Pump," *Proceedings of the IMechE, Part A, Journal of Power and Energy*, vol. 228 (5), pp. 574–584, 2014.

[11] Altare, G.; Rundo, M., "CFD Analysis of Gerotor Lubricating Pumps at High Speed: Geometric Features Influencing the Filling Capability", *Proceedings of the ASME/BATH 2015 Symposium on Fluid Power and Motion Control*, Chicago, IL (USA), October 12–14, 2015.

[12] Aldi, N.; Buratto, C.; Pinelli, M.; Spina, P.R.; Suman, A.; Casari, N., "CFD Analysis of a Non-newtonian Fluids Processing Pump," *Energy Procedia*, vol. 101, pp. 742–749, 2016.

[13] Iannetti, A.; Stickland, M.T.; Dempster, W.M., "A CFD Study on the Mechanisms which Cause Cavitation in Positive Displacement Reciprocating Pumps," *Journal of Hydraulic Engineering*, vol. 1 (1), pp. 47–59, 2015.

[14] Iannetti, A.; Stickland, M.T.; Dempster, W.M., "A CFD and Experimental Study on Cavitation in Positive Displacement Pumps: Benefits and Drawbacks of the 'Full' Cavitation Model," *Engineering Applications of Computational Fluid Mechanics*, vol. 10 (1), pp. 57–71, 2016.

[15] Srikanth, C.; Bhasker, C., "Flow Analysis in Valve with Moving Grids through CFD Techniques," *Advances in Engineering Software*, vol. 40 (3), pp. 193–201, 2009.

[16] Beune, A.; Kuerten, J.G.M.; van Heumen, M.P.C., "CFD Analysis with Fluid-Structure Interaction of Opening High-Pressure Safety Valves," *Computers & Fluids*, vol. 64, pp. 108–116, 2012.

[17] Zhang, S.C.; Zhang, Y.L.; Fang, Z.M., "Numerical simulation and analysis of ball valve three-dimensional flow based on CFD", IOP Conference Series: Earth and Environmental Science 15, 052024, 2012.

[18] Farrell, R.; Ezekoye, L.I.; Rain, M., "Check Valve Flow and Disk Lift Simulation Using CFD", *Proceedings of ASME Pressure Vessels and Piping Conference*, Hawaii (USA), July 16–20, 2017.

[19] Wang, G.; Zhang, L.; He, X.; Lei, Z.; Hu, G.; Li, R.; Wang, Y., "Dynamic Behavior of Reciprocating Plunger Pump Discharge Valve Based on Fluid Structure Interaction and Experimental Analysis," *PLoS One*, vol. 10 (10), pp. 1–20, 2015.

[20] Ma, Y.; Ni, Y.; Zhang, H.; Zhou, S.; Deng, H., "Influence of Valve's Lag Characteristic on Pressure Pulsation and Performance of Reciprocating Multiphase Pump," *Journal of Petroleum Science and Engineering*, vol. 164, pp. 584–594, 2018.

[21] Hwang, I.S.; Park, S.J.; Oh, W.; Lee, Y.L., "Linear Compressor Discharge Valve Behavior using a Rigid Body Valve Model and a FSI Valve Model," *International Journal of Refrigeration*, vol. 82, pp. 509–519, 2017.

[22] Tan, Q.; Pan, S.; Feng, Q.; Yu, X.; Wang, Z., "Fluid–Structure Interaction Model of Dynamic Behavior of the Discharge Valve in a Rotary Compressor," *Proceedings of the IMechE, Part E, Journal of Process Mechanical Engineering*, vol. 229 (4), pp. 280–289, 2014.

[23] Tao, W.; Guo, Y.; He, Z.; Peng, X., "Investigation on the Delayed Closure of the Suction Valve in the Refrigerator Compressor by FSI Modeling," *International Journal of Refrigeration*, vol. 91, pp. 111–121, 2018.

[24] van Rijswick, R.; Talmon, A.; van Rhee, C., "Fluid Structure Interaction (FSI) in Piston Diaphragm Pumps," *The Canadian Journal of Chemical Engineering*, vol. 94 (6), pp. 1116–1126, 2016.

[25] Pan, X.; Yang, S.; Shi, Y.; Liu, Y., "Investigation on the Dynamic Characteristics of Port Valves in a Diaphragm Pump for Exhaust Gas Treatment System by FSI Modeling," *IEEE Access*, DOI: 10.1109/ACCESS.2019.2914282, 2019.

[26] SAMOA Flow. Online catalogue for Diaphragm Pumps. http://www.samoaindustrial.com/flow/catalogo_directflo_en.html (accessed 21 November 2019).

[27] ANSYS-FLUENT User's Guide. Release 16.2. ANSYS, Inc., 2015.

[28] Wei, G., "An Implicit Method to Solve Problems of Rigid Body Motion Coupled with Fluid Flow," *Flow Science Inc., Technical note*, FSI-05-TN76, 2006.

[29] ANSYS-FLUENT Meshing User's Guide. Release 16.2. ANSYS, Inc., 2015.

[30] Menéndez Blanco, A., "Numerical Modelling of Volumetric Diaphragm Pumps", *Ph.D. Thesis* (in Spanish), University of Oviedo, Spain, 2017.